

## Research paper

# Direct observation of crack formation mechanisms with *operando* Laser Powder Bed Fusion X-ray imaging

Hossein Ghasemi-Tabasi<sup>a,\*</sup>, Charlotte de Formanoir<sup>a</sup>, Steven Van Petegem<sup>b</sup>, Jamasp Jhabvala<sup>a</sup>, Samy Hocine<sup>b,c</sup>, Eric Boillat<sup>a</sup>, Navid Sohrabi<sup>d</sup>, Federica Marone<sup>d</sup>, Daniel Grolimund<sup>d</sup>, Helena Van Swygenhoven<sup>b,c</sup>, Roland E. Logé<sup>a</sup>

<sup>a</sup> Thermomechanical Metallurgy Laboratory (LMTM) – PX Group Chair, École Polytechnique Fédérale de Lausanne (EPFL), CH-2002 Neuchâtel, Switzerland

<sup>b</sup> Photons for Engineering and Manufacturing, Paul Scherrer Institute, PSI, Forschungsstrasse 111, 5232 Villigen, Switzerland

<sup>c</sup> Neutrons and X-rays for Mechanics of Materials, IMX, École Polytechnique Fédérale de Lausanne (EPFL), Route Cantonale, 1015 Lausanne, Switzerland

<sup>d</sup> Swiss Light Source, Paul Scherrer Institute, 5232 Villigen, Switzerland

## ARTICLE INFO

## Keywords:

Laser powder bed fusion  
Operando X-ray imaging  
Ni superalloy  
Cracking  
Segregation

## ABSTRACT

Laser powder bed fusion (L-PBF) is a versatile additive manufacturing process that can print geometrically complex metal parts for a variety of applications. However, poor control of defect formation during processing hampers its widespread industrial adoption. Many materials suffer from a high crack susceptibility during L-PBF, which results in degraded mechanical properties, and is an obstacle to the certification of critical parts. In order to unveil the mechanisms of crack formation in a prone-to-cracking nickel-based superalloy, we employ high-speed synchrotron X-ray imaging in combination with a miniaturized L-PBF set-up that reproduces real processing conditions. This unique set-up provides *operando* imaging of crack formation during L-PBF. Complementary post-mortem inspection of crack morphology and thermal simulations supported by *operando* X-ray diffraction-based measurements of the temperature evolution allow to identify the cracking mechanism and to differentiate solidification cracking from liquation.

## 1. Introduction

Additive Manufacturing (AM) refers to different technologies that produce three-dimensional parts in a layer-by-layer mode. Due to its high technological and economic impact, the interest for AM has increased dramatically in recent years [1]. Laser Powder Bed Fusion (L-PBF), also known as Selective Laser Melting (SLM), is a highly versatile, and one of the most studied AM processes for metals. It enables the manufacturing of very complex metallic objects by selectively melting successive layers of powder based on a computer-aided design (CAD) file. From a metallurgical point of view, the complex thermal history that the material undergoes during L-PBF differs substantially from conventional processing. It is characterized by a succession of fast melting, fast solidification (cooling rates  $\sim 10^6$  °C.s<sup>-1</sup>), and cyclic remelting or reheating in the vicinity of the melt pool. The thermal gradients induced by the process and the large degree of shrinkage occurring during solidification create high residual stresses and favor crack formation [2–6].

The CM247LC nickel-based superalloy is a  $\gamma'$ -strengthened Ni superalloy, which is of particular interest due to its excellent mechanical, creep, wear, and oxidation properties at both ambient and elevated temperatures [7–10]. However, this alloy contains high amounts of Al and Ti and is considered vulnerable to cracking due to L1<sub>2</sub>, Ni<sub>3</sub> (Al, Ti) precipitation [11,12]. In literature, several mechanisms are reported to be responsible for cracking during the manufacturing of CM247LC alloy. Solidification cracking, liquation cracking and ductility dip cracking (DDC) are the main mechanisms that have been suggested [13–18].

Solidification cracking occurs in the last stages of solidification, due to a combination of solute-rich liquid entrapment between solid interfaces and tensile residual stresses that pull the interfaces apart [13–15,19,20]. Liquation cracking results from the micro-segregation that takes place during fast solidification, which locally lowers the solidus point. When an adjacent line scan or additional layer is processed, localized melting and associated cracking occur in the heat-affected zone [13–15,21]. Finally, ductility reduction in a  $[0.5 T_{\text{solidus}} - T_{\text{solidus}}]$  temperature range has been reported in Ni-based superalloys. As is

\* Corresponding author.

E-mail address: [hossein.ghasemitabasi@epfl.ch](mailto:hossein.ghasemitabasi@epfl.ch) (H. Ghasemi-Tabasi).

<https://doi.org/10.1016/j.addma.2022.102619>

Received 29 September 2021; Received in revised form 23 December 2021; Accepted 9 January 2022

Available online 12 January 2022

2214-8604/© 2022 The Author(s).

Published by Elsevier B.V. This is an open access article under the CC BY-NC-ND license

(<http://creativecommons.org/licenses/by-nc-nd/4.0/>).

the case for solidification and liquation cracking, the presence of residual stress within this temperature range results in the so-called “ductility dip cracking” (DDC) [16–18,22].

Kalentic et al. [13] observed solidification and liquation cracks in as-built CM247LC samples. Griffiths et al. [14] suggested that micro-cracking in CM247LC was attributed to both solidification and liquation cracking. Gleeble experiments on as-built CM247LC L-PBF samples showed that a liquation cracking mechanism is most likely active in the heat-affected zone of laser tracks. Both numerical simulations and chemical analysis suggested that Hf influences the freezing range of the alloy and makes it susceptible to cracking.

Liquation cracking was also reported in as-built samples of IN738LC (another  $\gamma'$ -strengthened Ni superalloy) [23]. The presence of low melting point alloying components in the vicinity of the crack surface constitutes evidence of this cracking mechanism [14,16,23].

Carter et al. [17] studied L-PBF-printed CM247LC samples and observed high-angle grain boundaries near the cracks, thus concluding that DDC is the main cracking mechanism in this alloy. The microstructure consists of columnar grains containing slightly misorientated cells elongated along the build direction. TEM analysis revealed the presence of small carbides within the cells, inter- and intra-cellular  $\gamma'$  precipitates, and a high density of dislocations at the grain and cell boundaries. These observations support the DDC mechanism [16,18].

The origin of cracking in additively manufactured  $\gamma'$ -strengthened Ni-based superalloys is thus still a matter of debate. So far, only post-mortem crack examinations have been performed and no observation of cracking during additive manufacturing of CM247LC samples in real conditions is reported in the literature. As demonstrated for other materials, in-situ analysis is a useful approach to study a variety of phenomena, such as crack formation, that take place during laser processing [24,25]. In particular, in-situ X-ray imaging is a powerful technique to investigate the formation of defects in metals during thermal processing. In recent years, several fast in-situ radiography measurements have been performed during laser processing. These experiments mostly focus on the study of melt pool dynamics [26–41], on the formation and elimination of pores [27,30,42–45], and on the generation of spatters [27, 46–51]. Despite its importance for the final mechanical integrity of L-PBF parts, there exists little literature on the in-situ observation of crack formation. Preliminary work demonstrated the feasibility of observing cracks in an aluminum alloy 6061 [52,53]. Their geometry and interaction with porosities was emphasized from single laser line tracks, with however a simplified setup consisting of cuboidal solid specimens with no powder layer on top [53]. Whenever the aforementioned in-situ studies use a powder-bed system, the chosen configuration faces several limitations. It systematically consists of two plates that are transparent to X-rays and separated by a few hundred microns, between which a substrate is sandwiched. In most cases, a 100  $\mu\text{m}$ -thick single layer of powder is manually applied on top of the substrate [26,27,37, 38,43], whereas in other cases the X-ray experiments are directly performed on the bare substrate, without any powder bed, to enhance clarity [28,37,43,53]. This two-plate setup can be considered as a quasi-2D configuration, which captures the evolution of a single layer melt track rather than the whole 3D character of the L-PBF process. In this type of setup, heat extraction from the melt pool may differ from what takes place in larger three-dimensional parts which consist in the superposition of multiple layers. Regardless of the mechanism at play, most crack formation mechanisms during L-PBF are promoted by tensile residual stresses, which tend to accumulate through several layers. It is therefore essential to monitor the printing of several layers to observe cracking during the L-PBF process. To that end, a miniaturized L-PBF device [54,55] optimized for usage at synchrotron beamlines and reproducing at a small scale close-to-real processing conditions in the three dimensions, is employed in the present study. *Operando* radiography, combined with post-process SEM, EBSD and EDX analyzes and thermal simulations, provides valuable information on the conditions of crack initiation and the possible cracking mechanisms taking place

during processing. Complementary *operando* X-ray diffraction experiments are used to monitor the evolution of temperature during processing and relate it to the simulated results.

## 2. Experimental method

### 2.1. Materials and fabrication

Commercial gas-atomized CM247LC powder provided by Oerlikon Metco (Pfaeffikon, Switzerland) was used in this study. Powder size distribution was 15 – 45  $\mu\text{m}$  with a  $D_{50}$  of approximately 30  $\mu\text{m}$ . The chemical composition of the powder is listed in Table 1 [14]. The *operando* radiography experiments were performed with a miniaturized L-PBF device developed at the Paul Scherrer Institute (Switzerland). It mimics a commercial L-PBF device while being optimized for usage at synchrotron beamlines, thanks to its relatively small dimensions (height: 520 mm, lateral dimensions: 280 mm and 260 mm) and weight (25 kg) and to the presence of two openings (at the back and front) allowing the incoming X-ray beam to enter the backside through a 100  $\mu\text{m}$ -thick glassy carbon window, interact with the specimen and exit at the front through a 500  $\mu\text{m}$ -thick glassy carbon window. The surface of the build plate is 12  $\times$  12  $\text{mm}^2$  while the total build height is limited to about 5 mm. A more detailed description of the device can be found in [54,55]. The laser source is a 500 W redPOWER® continuous wave (CW) Fiber Laser (SPI Lasers Ltd, UK), operating at a wavelength of 1070  $\pm$  10 nm. The laser beam is collimated as a parallel Gaussian beam into a 2-axis SuperScan III deflection-scanning unit (Raylase GmbH, Germany) with a 15 mm input aperture. Two fused silica mirror galvanometers allow scanning the laser beam over the power bed. The beam is focused down to a  $\phi$ 100  $\mu\text{m}$  spot size through an F-Theta lens (Sill Optics, Germany). Both laser and scanning unit are controlled via an SP-ICE-3 board and the WeldMARK software (Raylase GmbH, Germany). Before and during operation, the chamber is flushed with Ar-gas. Furthermore, on the recoater a gas-outlet is mounted, which blows Ar-gas over the powder bed.

The laser process parameters were determined based on ex-situ analysis preliminary to the *operando* experiments (Table 2).

The printed samples were cut along the build direction and polished mechanically by SiC papers up to 2500 grit size and then polished by diamond suspension until 1  $\mu\text{m}$ . To reveal the microstructure around the cracks, polished samples were etched with the Kalling solution (25 ml ethanol + 25 ml HCl + 2.25 g  $\text{CuCl}_2$ ) for one minute. Crack morphology analysis was done using a Zeiss-Gemini2 field emission scanning electron microscope. SEM-EDX analysis was performed at 15 keV. Electron Backscatter Diffraction (EBSD) maps were acquired at 25 kV using the same microscope equipped with the Symmetry camera and Aztec acquisition software (Oxford instrument). The maps were acquired with the step size of 0.5  $\mu\text{m}$  and acquisition rate of 400 Hz with detection of 10 bands, with a gain of 2 in the mode speed 1.

### 2.2. Operando synchrotron X-ray imaging

The *operando* X-ray imaging experiments were performed at the TOMographic Microscopy and Coherent rAdiology experimentTs (TOMCAT) beamline of the Swiss Light Source using an in-house built L-PBF device [54,55]. Fig. 1 displays a schematic view of the setup. The miniaturized L-PBF device was mounted on a dedicated stage and tilted by 20 degrees compared to the direction of the incoming X-ray beam. The edge of the powder bed was illuminated by a parallel X-ray beam with energies ranging between approximately 10 and 55 keV. The polychromatic radiation emerging from the source was filtered with 5 mm of Sigradur (50% power filter) and 0.525 mm of Si. The transmitted beam was recorded with a custom-made 4  $\times$  microscope [56], coupled to the in-house developed GigaFRoST detector [57]. This detector exhibits a 2016  $\times$  2016 pixels CMOS imaging chip with 11  $\mu\text{m}$  pixel size and 12-bit nominal dynamic range. Its novel readout system provides

**Table 1**

Chemical composition of the CM247LC powder.

wt%	Al	W	Co	Cr	Ta	Hf	Ti	Mo	C	Fe	B	Zr	Ni
CM247LC	5.71	9.93	9.24	8.62	3.08	1.37	0.73	0.54	0.06	0.02	0.017	0.006	Bal

**Table 2**

Processing parameters.

Laser and material characteristics	
Spot diameter ( $1/e^2$ )	100 $\mu\text{m}$
Power	160 W
Scanning speed	220 mm/s
Hatch distance	100 $\mu\text{m}$
Scanning strategy	Bi-directional
Base plate material	316 L stainless steel
Pre-heating temperature	25 $^{\circ}\text{C}$
Layer thickness	40 $\mu\text{m}$

continuous and sustained data streaming up to almost 8 GB/s to a dedicated high-performance data backend server. To optimize the visibility of crack observation, the microscope was positioned at a relatively large distance from the sample (70 cm). This resulted in an enhanced contrast for edges. The experiments were performed at an acquisition frequency of 10 kHz. This was achieved by reducing the region of interest to  $672 \times 512$  pixels, equivalent to a field-of-view of  $1.85 \times 1.41 \text{ mm}^2$  (width  $\times$  height). The optics consist of the custom-made microscope with  $4 \times$  magnification and a high numerical aperture of 0.35,

resulting in an effective pixel size of  $2.75 \mu\text{m}$ . Prior to the *operando* radiography experiments  $8 \times 2 \times 0.4 \text{ mm}^3$  cuboids were printed near the edge of the build plate (Fig. 1c). During the *operando* radiography experiment, a single layer was printed with the same process parameters. Fig. S1 in the supplementary materials indicates some examples of printed CM247LC samples. All the acquired data were Flat-Field Corrected (FFC) using MATLAB R2018a [31] and an average flat-field image computed out of 10 consecutive frames. The contrast of corrected images was adjusted by Fiji and GIMP using color balance and color curve adjustment features. Supplementary Fig. S2 displays a picture of the mounted setup at the TOMCAT beam line of the Swiss Light Source.

As the sample is tilted compared to the incoming beam, the interpretation of the radiographs is not straightforward. Fig. 2 displays a 3D schematic of the *operando* experiment for the first and final printed track of a given layer, together with representative features in the 2D projected images. This includes powder particles, solidified material, spatters, pores, and cracks. A more detailed discussion on the observed contrasts of these features can be found in the Supplementary materials S3.

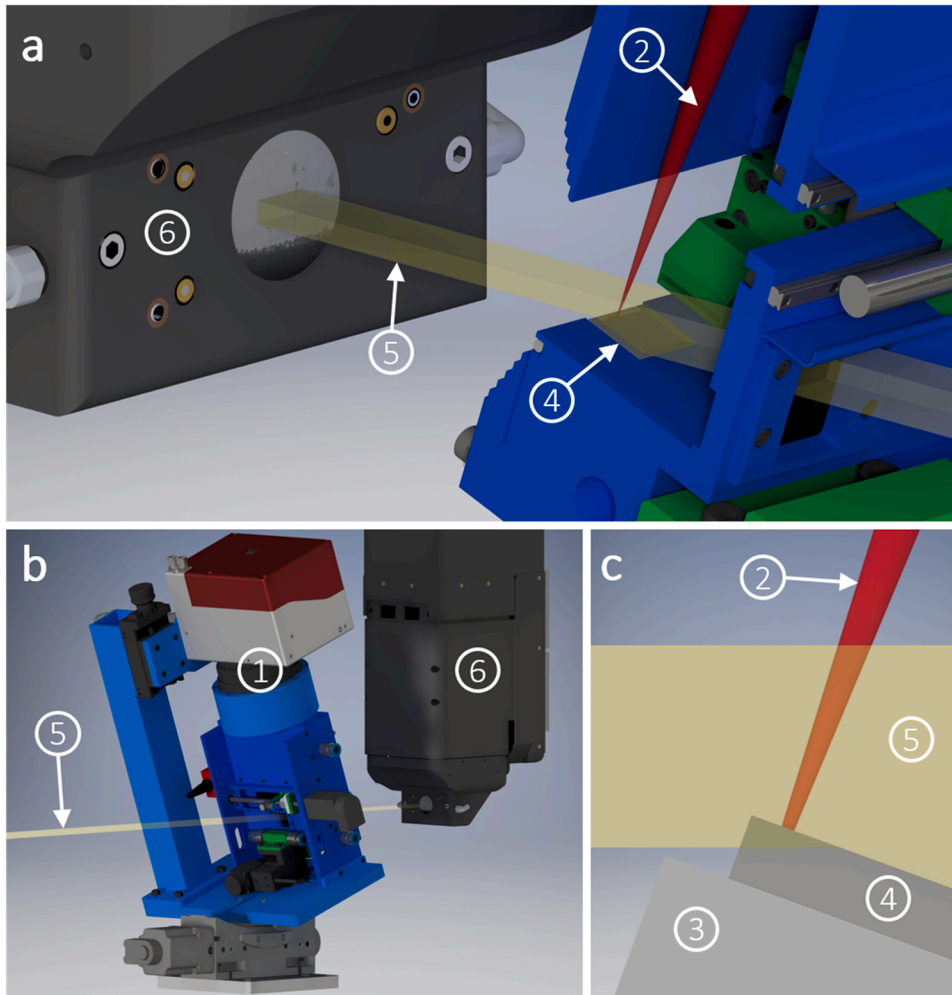


**Fig. 1.** Schematic view of the *operando* radiography setup at the TOMCAT beamline. a), b) Open build chamber of the miniaturized L-PBF machine and the camera in two different views, and c) zoom on the build plate and the printed sample to highlight the volume in which data is acquired during the *operando* experiment. A 2-axis scanning head (1) deflects the laser beam (2) on to a  $12 \times 12 \text{ mm}^2$  build plate (3) and the sample (4). A parallel X-ray beam (5) passes through the sample (Fig. 1c) and reaches the microscope (6).

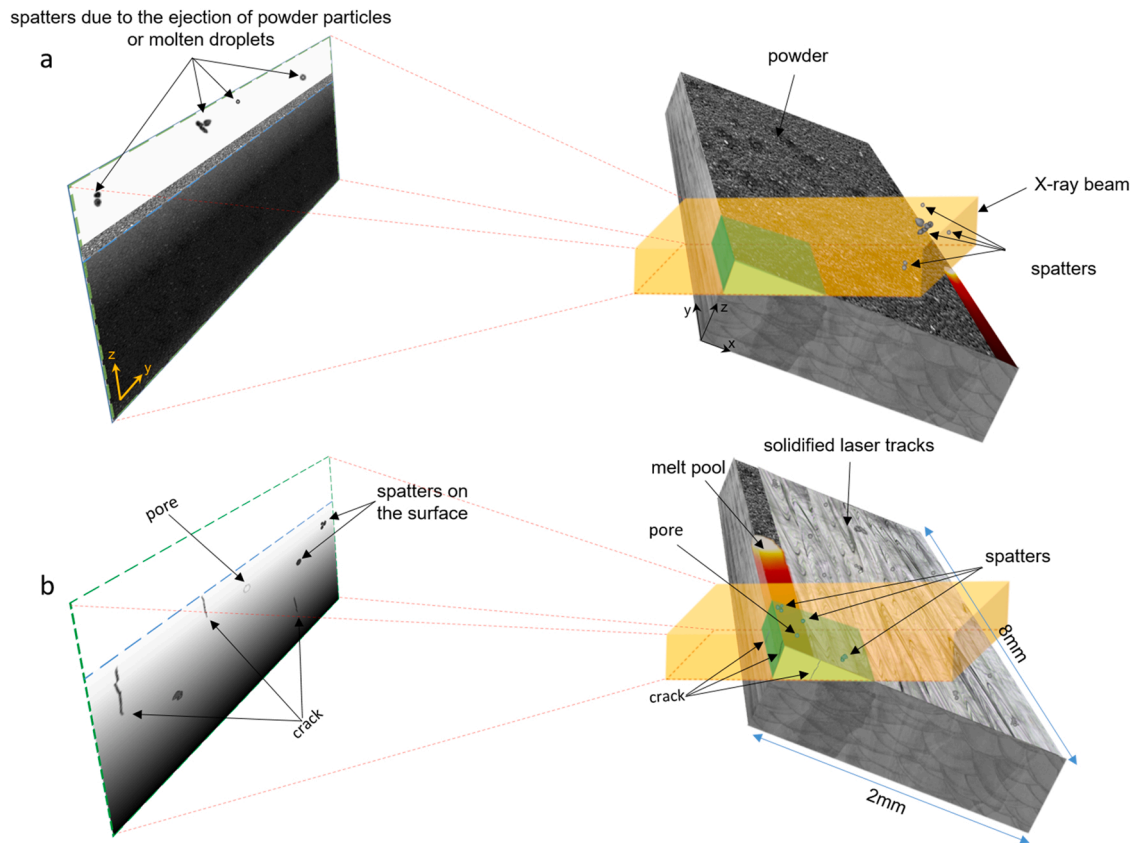


**Fig. 2.** 3D schematic of the *operando* radiography experiments. Two representative cases, i.e. at the beginning (a) and at the end (b) of the printing of a layer, are depicted to illustrate the type of features that can be observed: spatters and powder particles, cracks and pores. The volume of material analyzed during the experiment is highlighted in green and the corresponding projected 2D image can be seen on the left. Powder particles on the top surface exhibit a darker contrast, whereas pores appear brighter. Cracks exhibit a dark contrast, as explained in [Supplementary materials S3](#). At the beginning of the process, (a) during the printing of the first tracks at the back of the sample, some spatters appear in the images as a result of the ejection of “cold” powder particles and “hot” molten metal droplets [58] in the vicinity of the melt pool. After printing the last tracks near the edge of the sample, i.e. in the green volume, cracks and pores appear in this region and can be observed in the 2D images (b). In the last tracks (b), due to denudation effects, a much lower amount of powder particles is present on the top surface compared to the first tracks (a). For visibility purposes the different features (melt pool, cracks, pores, X-ray beam) represented in the schematic are not at the right scale.

### 2.3. Operando synchrotron X-ray diffraction

The *operando* X-ray diffraction experiments were performed at the MicroXAS beamline of the Swiss Light Source (SLS) using the same L-PBF device and processing parameters as for the X-ray imaging experiments. The X-ray beam had an energy of 17 keV and was focused to a projected spot size of  $80 \times 80 \mu\text{m}^2$ . [Fig. S3](#) in Supplementary materials displays a picture of the L-PBF device mounted at MicroXAS. The experiments are performed in reflection mode, where the X-ray beam is positioned in the center of the sample. The diffracted beam is recorded by a 1 M EIGER detector, developed at the Paul Scherrer Institute. During printing, 4-bit 2D diffraction patterns are recorded at a frequency of 20 kHz. Azimuthal integration was done with pyFAI, resulting in 1D images with an angular range between  $10^\circ$  and  $70^\circ$ .

[Fig. S3](#) in Supplementary materials shows a representative ‘intensity vs diffraction and time’ plot. When the laser passes the area illuminated by the X-ray beam, the diffraction peaks change their position due to thermal expansion and contraction. This can be expressed as a change in lattice strain, which, in turn, is converted into a change in temperature using temperature-dependent thermal expansion coefficients [59,60]. Here, it is assumed that the thermal effects on the lattice constant are significantly larger compared to the effects of residual stresses and chemical composition [54].

### 2.4. Numerical simulations

A dedicated numerical simulation software has been developed to model the temperature distribution during the L-PBF process. Stress calculation is not implemented in the current version of the FEM code. The powder bed is considered as a homogeneous medium, with effective properties such as absorptivity, optical penetration depth, density, thermal conductivity, etc. Thermophysical properties vary according to the material state (powder, solid, and liquid). The absorptivity of powder particles is 57%, as measured with a Perkin Elmer Lambda900 spectrophotometer at 1070 nm wavelength [61,62]. Thermophysical properties and their evolutions with temperature are taken from [14, 63–66]. To validate simulated temperatures, the values are compared with *operando* x-ray experiments. The simulation is done using the same process parameters and scanning strategies as for the *operando* experiments. Simulated temperatures are averaged over the x-ray beam probed zone, in the same way as the *operando* x-ray experiment does. During the *operando* experiments, the temperature in the liquid phase cannot be calculated using the diffraction data. Therefore, reported experimentally measured temperatures correspond to the solid state only, and are significantly below the simulated ones for the liquid state. More details on the finite element simulation framework are available in a recently published paper [61].



### 3. Results and discussion

#### 3.1. Operando observation of crack formation

During the experiments, two distinct crack-related features could be observed: 1) formation, growth, and remelting of cracks after interaction with the melt pool, and 2) growth of existing cracks after interaction with the heat-affected zone (HAZ).

Fig. 3 shows five snapshots during the printing of two adjacent tracks. The contrast was adjusted to highlight pores and cracks; spatters are not visible here. At  $t = t_0$  the laser passes position A with the scanning direction to the left. After 2.7 ms, (not shown here, see Supplementary Movie 1) a crack appears and grows towards the top surface. The fully-grown crack after 4.4 ms can be seen in Fig. 3c. Similar features were found in other samples, as illustrated in Supplementary Fig. S7. During printing of the adjacent track, the laser reaches again the (2D-projected) position A after 13.5 ms (Fig. 3e). After the laser has passed, the top part of the crack disappears, indicating that it was remelted (Fig. 3f). However, with a 2.9 ms delay (see Supplementary Movie 1), the crack starts growing again towards the top surface (Fig. 3g).

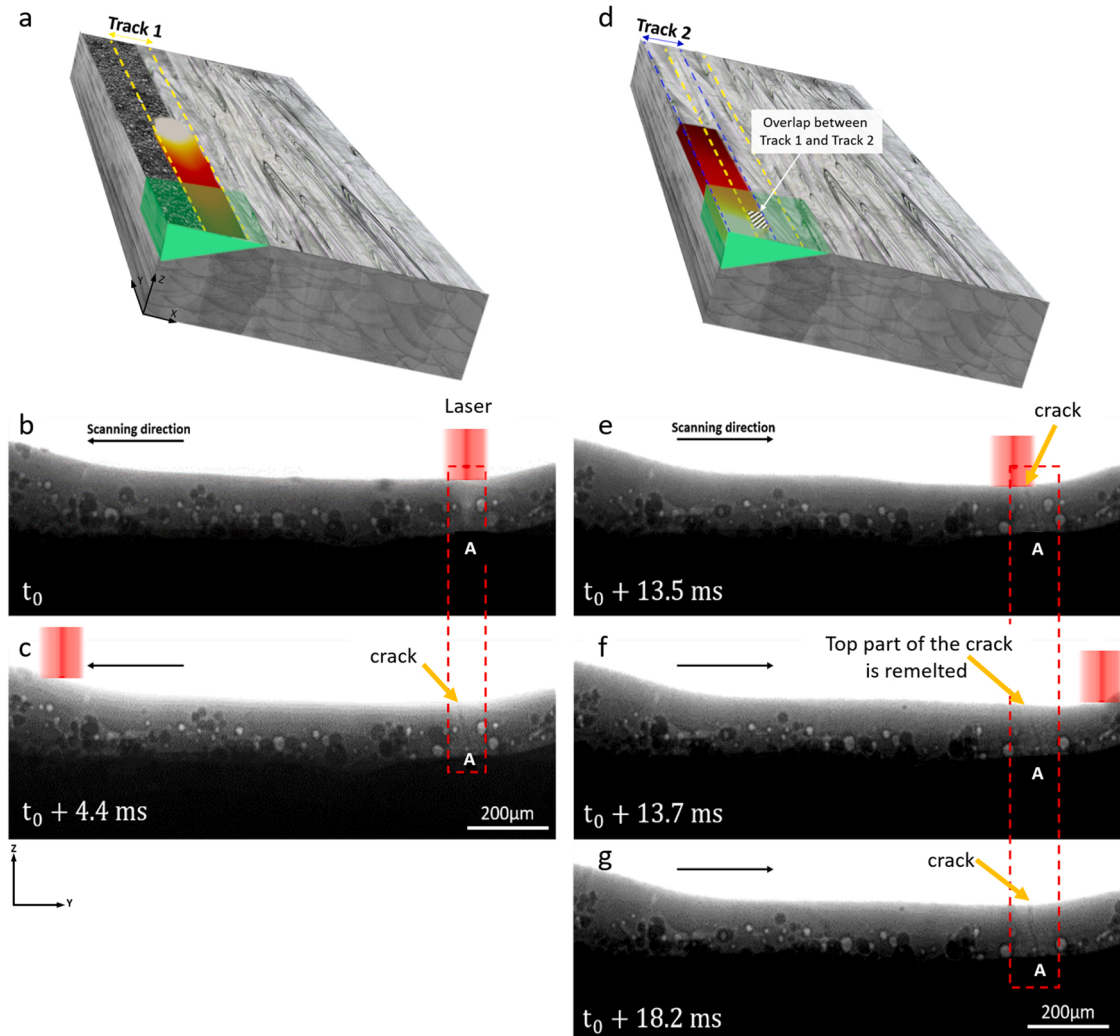


**Fig. 3.** Radiographs acquired during L-PBF of CM247LC. a) The position of the track (Track 1) observed in b) and c) is shown schematically. b) At  $t = t_0$ , the laser reaches point A. The crack starts appearing at the same location 2.7 ms later. c) The crack is clearly visible at  $t = t_0 + 4.4$  ms. d) The position of the track (Track 2) observed in e), f) and g) is shown schematically. e), f) During printing of the next line scan, the crack is partially remelted. Track 2 remelts the top part of the crack. Considering the overlap between two adjacent tracks, the striped part in d) indicates the zone in which the crack formed. The crack starts growing again towards the surface with a 2.9 ms delay. g) A radiograph at  $t = t_0 + 18.2$  ms clearly shows the fully regrown crack. See Supplementary Movie 1 for a better observation of the crack formation.

In Fig. 4a, a crack is already present in position B. When the laser passes in B (Fig. 4b), no visible change in the morphology and length of the crack is observed. Knowing the exact location of the crack with respect to the laser along the depth of the sample is not straightforward in transmission mode. However, as the crack does not appear to be remelted by the laser in Fig. 4b, it can be assumed that the crack in B is not located in the laser beam path but rather in an adjacent track, i.e. in the HAZ. A similar interaction between an existing crack and the HAZ can be seen in Supplementary Fig. S8. After 2.2 ms, the crack starts growing towards the surface; the fully grown crack is visible in Fig. 4c. During the next laser track, when the laser reaches point B (Figs. 4d and e), the top part of the crack disappears, indicating that the crack is now located in the laser beam path and is being remelted. After 2.4 ms, the crack propagates back to the surface; the fully grown crack is visible in Fig. 4f.

Supplementary material related to this article can be found online at [doi:10.1016/j.addma.2022.102619](https://doi.org/10.1016/j.addma.2022.102619).

#### 3.2. Mechanisms of crack formation

The *operando* monitoring experiments reported in Fig. 3 and Fig. 4

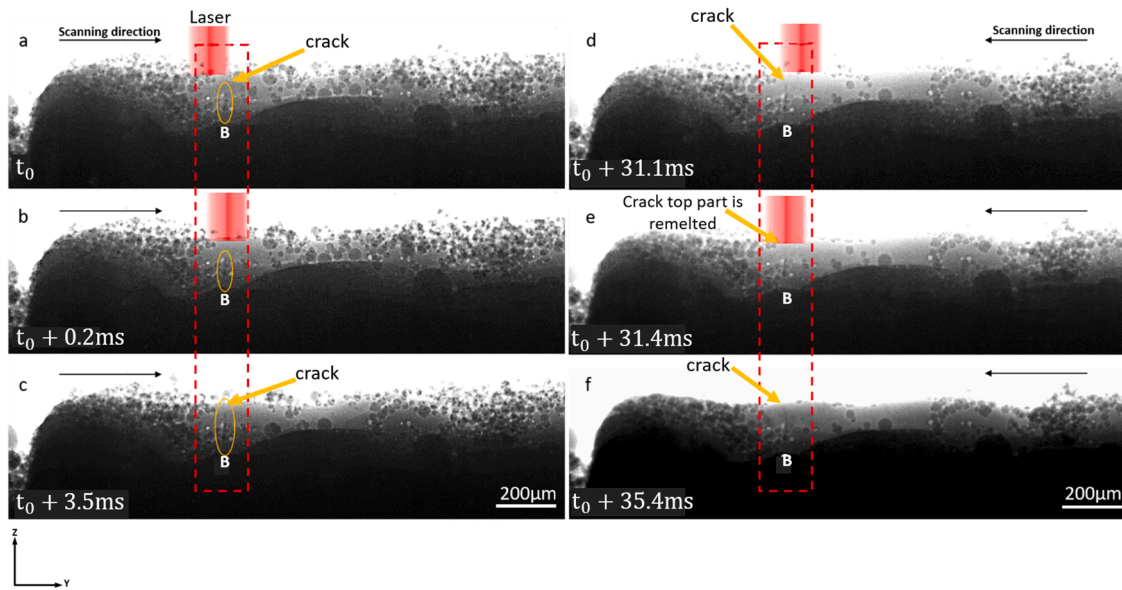


**Fig. 4.** Radiographs acquired during L-PBF of CM247LC. a) At  $t = t_0$ , a crack is visible in B and b) the laser reaches the B position 0.2 ms later but does not appear to alter the crack morphology. 2.2 ms after the laser passes point B, the crack starts growing. The fully-grown crack is visible in c). d), e) During the next laser track, the top part of the crack is remelted, and with a 2.4 ms delay the crack starts growing again and reaches the surface. The fully-grown crack is clearly observable in f). See [Supplementary Movie 2](#) for a better observation of the crack formation.

illustrate the occurrence of crack formation or crack growth.

In addition to direct observation during the manufacturing process, post-mortem SEM analysis and numerical simulations have been used to provide a better understanding of the cracking mechanisms at stake.

SEM analysis of cracks located near the top surface of the sample reveals a dendritic morphology, indicative of fracture occurring in the presence of a liquid phase [11,14]. As highlighted in Figs. 5a and b, crack propagation occurs preferentially along grain boundaries. The SEM-EDX analyses reported in Figs. 5c and d indicate local enrichment

in Ta and Hf at the edge of cracks. It should be noticed that these SEM-EDX analyses are obtained after processing. It can be reasonably assumed that the successive L-PBF thermal cycles occurring after cracking partially homogenize the material chemistry in the crack vicinity, resulting in an underestimation of the micro-segregation that actually took place during solidification [14].

Fig. 6 displays cumulative disorientation across the grain boundaries where cracks formed in the top region of the part during the *operando* experiment. The results confirm that all observed cracks propagated

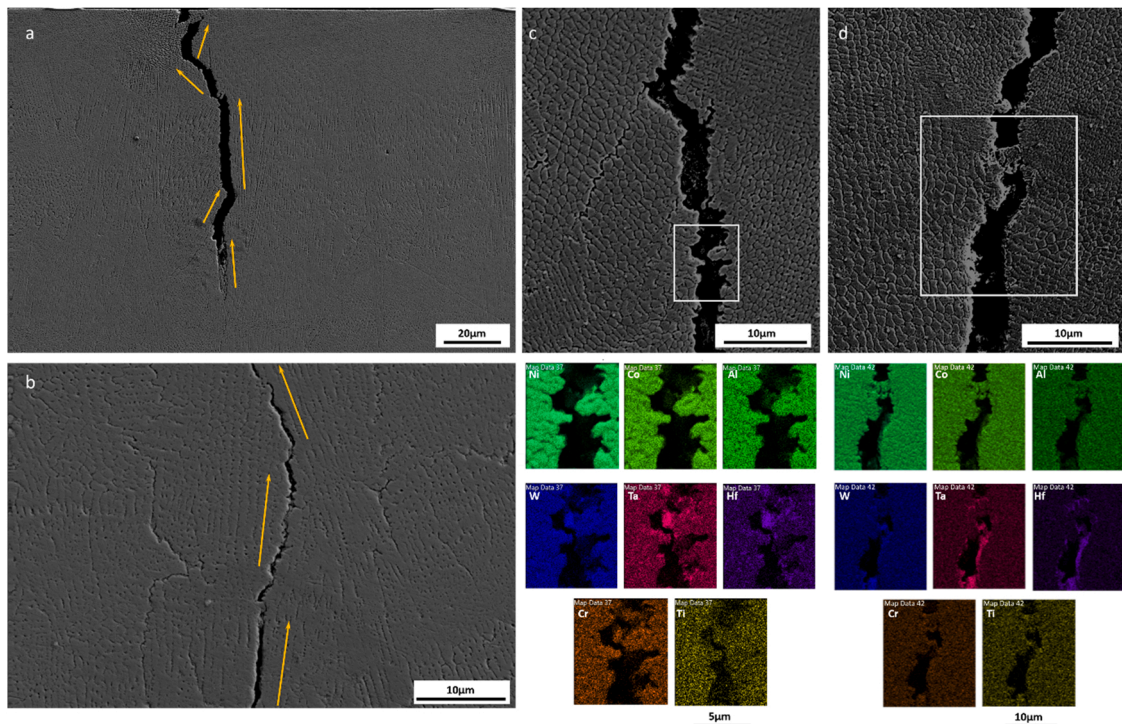


**Fig. 5.** a, b) SEM secondary electron images of the sample printed during the *operando* experiment (Y-Z cross section) indicating preferential propagation of cracks along grain boundaries (yellow arrows). c, d) SEM-EDX analysis highlighting element distribution in the vicinity of the cracks.

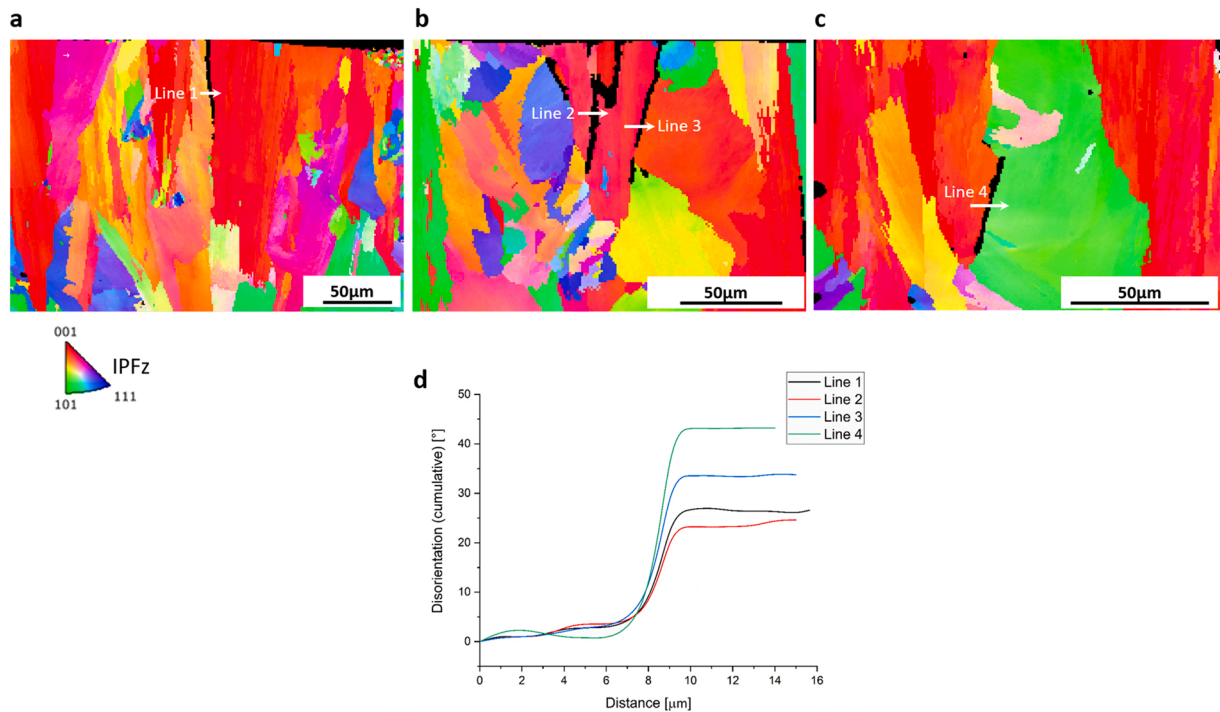


**Fig. 6.** a,b,c) EBSD orientation maps (IPFz) of the printed samples and d) cumulative disorientation across cracked grain boundaries close to the top surface in samples built during the *operando* experiment (Y-Z cross section). (For interpretation of the references to colour in this figure, the reader is referred to the web version of this article)

along high angle grain boundaries, i.e. the crystallographic misorientation between the neighboring grains was higher than 15°.

The segregation of Hf and its effect on the solidification behavior of CM247LC has been investigated by Griffiths et. al [14]. Their calculated liquidus and solidus temperatures suggest that micro-segregation happens during the L-PBF process and can locally increase the solidification range from 150° to 525°C, depending on the chemical composition of the segregated area. The solidus temperature can be locally reduced from 1249° to 858°C. Therefore, during the last stage of solidification, crack formation can result from the entrapment of solute-rich liquid between solid interfaces and the tensile residual stresses induced by solidification shrinkage and thermal gradients [11]. The misorientations measured across the cracks (Fig. 6) are in accordance with the solidification cracking mechanism [67,68]. Higher-angle grain boundaries remain wetted at lower temperatures (due to increased boundary energy), which in turn increases the solidification cracking susceptibility [69].

In order to relate crack formation with the thermal history of the material, the temperature evolution during LPBF processing of the *operando* experiment was evaluated using a finite element code described in [61,70]. This model takes into account the presence of three different material states: bulk solid, powder, and liquid. It is a thermal model (i.e. no mechanical computation), and is meant to provide the exact thermal history of a given location in the material, with potential changes of state depending on the distance to the laser track. The simulation set-up is illustrated in Fig. 7a, while simulation results are reported in Figs. 7b, c, and d (black curve). Experimental temperatures in Fig. 7d are estimated from *operando* X-ray diffraction measurements obtained under the same processing conditions as the *operando* X-ray imaging experiments. They are calculated from the measured change in lattice spacing, using the thermal expansion coefficients tabulated in [59]; in the solid state (the liquid phase temperature cannot be measured), they validate quite accurately the simulated average temperature evolution (in the X-Ray probed zone) during processing. Based on this simulated thermal field, the time required for solidification at a

point A located on the surface, at the center of the melt track, is estimated to 2.65 ms (Fig. 7c, black curve).

Direct observation of cracking combined with numerical simulations and post-mortem chemical and microstructural analyses of the cracks confirm that cracks observed in Fig. 3, and Figs. 4e, f (also Fig. S7, and point D in Fig. S8 in the supplementary materials), which formed about 2–3 ms after laser exposure, originate from such a solidification cracking mechanism: (i) cracks are first melted (i.e. they are not in the HAZ, but correspond to a zone in the melt pool, similar to point A in Fig. 7), and (ii) the time for them to reappear is consistent with the end of the calculated solidification process.

Fig. 8.a provides a schematic view of the melt pool formation during L-PBF. A few ms after the laser passes a specific point, solidification starts (Fig. 8-b). Micro-segregation occurs at the scale of the melt pool [14,71] and increases the solidification range, while high tensile stresses accumulate in the vicinity [72–74]. These conditions promote solidification cracking, illustrated in Fig. 8.c by two examples of solidification cracks that were captured during *operando* experiments, with a delay of about 2–3 ms between laser-material interaction and crack formation.

Micro-segregation of elements during solidification of the alloy results in grain boundaries having a depressed solidus point due to the change in chemical composition. When these boundaries are subjected to elevated temperatures in the HAZ, they liquefy and become susceptible to tearing: this is the liquation mechanism. Using Gleeble experiments, Griffiths et. al [14] suggested that cracks in the solid state of CM247LC samples form after a liquid film in segregated regions of the HAZ has been pulled apart by the tensile residual stresses. Fig. 6c (red curve) indicates the temperature evolution at a location B (100 μm below the surface, the layer thickness being 40 μm), during the printing of three successive line tracks. When considering here a standard hatching distance (100 μm), the heat-affected zones in previous layers and adjacent tracks both reach sufficiently high temperatures to locally melt the segregated zones. A different scanning strategy would influence the temperature field and result in a different HAZ volume [75–78]. Fig. 9.a is a schematic view of the liquation cracking mechanism in the



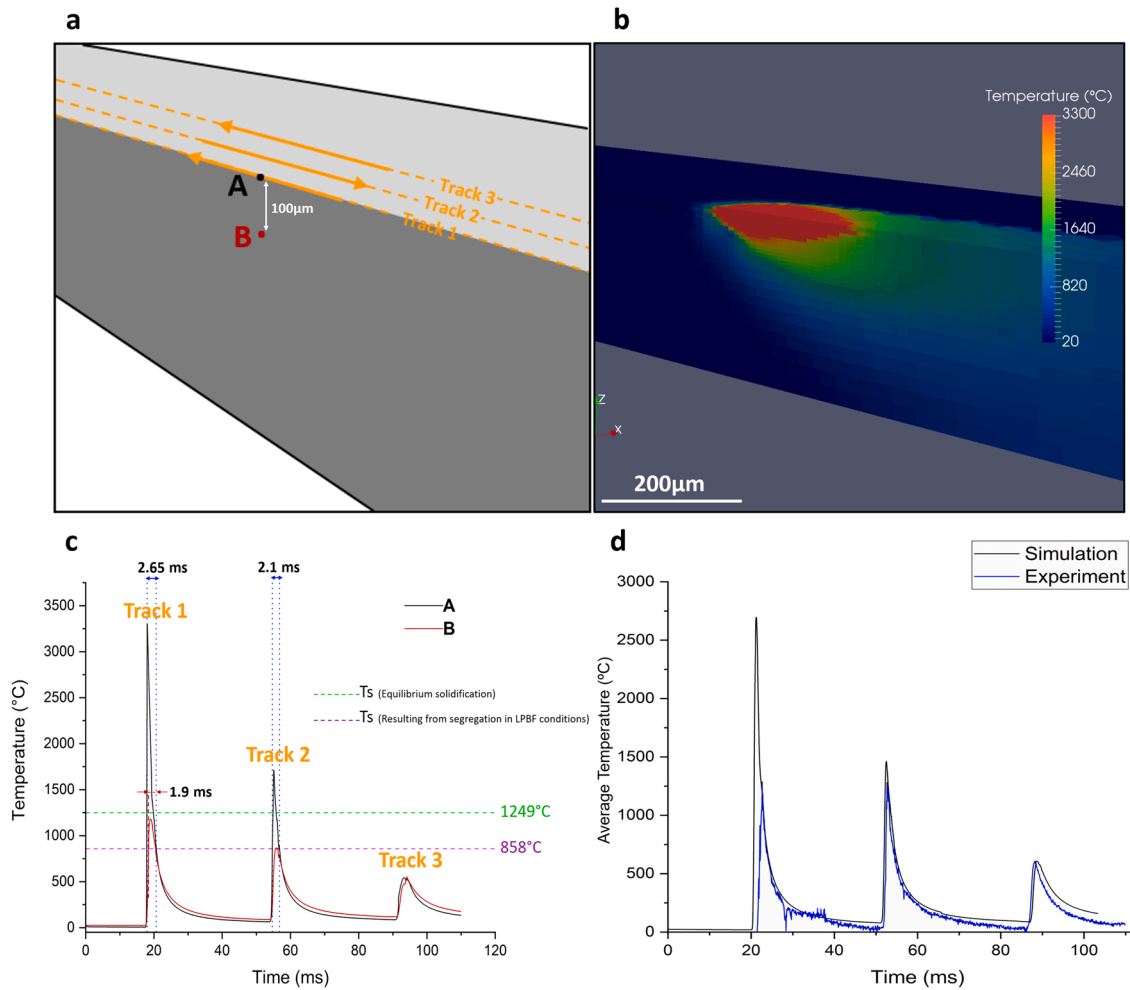


**Fig. 7.** Finite element simulation indicating the temperature evolution at the melt pool scale in the process conditions corresponding to the *operando* L-PBF experiments. a) Reference positions A and B with respect to the three laser line tracks considered in the simulation, b) temperature distribution when the laser reaches point A, c) temperature evolution at point A and point B, during successive printing of the three adjacent tracks. The solidification time at point A is 2.65 ms after the first laser pass, which is comparable to the measured times for crack formation in the *operando* experiments. In point B (located in the heat affected zone), heat transfer to the previously solidified layer is sufficient to locally melt segregated zones ( $T > 858^\circ\text{C}$ ). d) Simulated temperatures averaged over the X-ray probed zone compared with the experimental values, from X-Ray diffraction. The spike in the FEM-predicted temperatures corresponds to the first track where a melt pool (liquid phase) forms. Measured temperatures only refer to the solid state and are therefore significantly below the simulated peak values of the first track.

HAZ of a laser track, where cracks form as a result of local melting of solute-enriched grain boundaries. This cracking mechanism is observed in Fig. 4c (as well as at point E in Fig. S8 in the Supplementary materials) where a pre-existing crack located in the HAZ grows about 2.2 ms after the laser beam passes.

We conclude that combining *operando* experiments with numerical simulations of LPBF can provide evidence of the exact conditions in which either solidification or liquation cracking occurs in CM247LC. Once these conditions have been identified, they can be used to test criteria for solidification cracking. Previous studies in the fields of welding and casting have already proposed formulations, e.g. the grain boundary liquid film (GBLF) [79] and the Rappaz-Drezet-Gremaud (RDG) criteria [80].

According to the above cracking criteria, printing crack-free samples would in principle require slower solidification velocities [81]. However, drastic changes in the laser energy density can lead to other kinds of defect such as part delamination, keyhole instability, and lack-of-fusion porosities [14,81]. Preheating methods have been used as a strategy to reduce thermal gradients, thermal stresses and solidification velocities. For example, Ramsperger et al. [82] managed to print crack-free CMSX-4 samples using the electron beam bed fusion process with high temperature preheating ( $1040^\circ\text{C}$ ). The same approach was

used in L-PBF by Hagedorn et al. [83], who preheated the build plate at  $1200^\circ\text{C}$  and obtained crack-free CM247LC. However, the majority of L-PBF machines does not have the ability to pre-heat at such high temperatures. Alternatively, alloy-by-design (ABD), i.e. designing new grades of  $\gamma/\gamma'$  nickel-based superalloys specifically for AM processes, could be a promising approach, considering that most of the  $\gamma/\gamma'$  nickel-based alloys currently considered in AM were initially designed for conventional processes such as casting [10].

#### 4. Summary

In summary, *operando* radiography allows the observation of crack formation during L-PBF of the CM247LC nickel-based superalloy. Together with *operando* X-Ray diffraction and numerical simulations, these experiments provide direct evidence of both solidification and liquation cracking mechanisms, with the possibility to distinguish one from the other. We expect that a better understanding of cracking achieved in this study will stimulate the development of more accurate numerical simulations of the L-PBF process, cracking criteria, and new approaches to achieve crack-free L-PBF nickel-based parts, such as to unravel the full industrial potential of AM technologies for these alloys. Furthermore, the unique *operando* experimental setup employed here



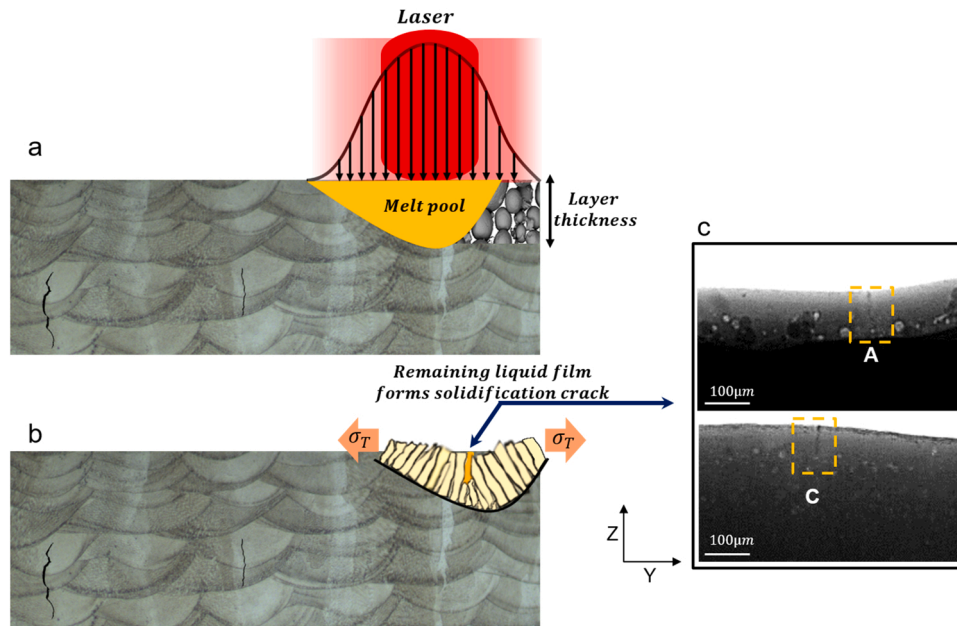


**Fig. 8.** a) Schematic view of the melt pool formation during the L-PBF process. b) Due to fast cooling rates during the final stages of solidification, solute-rich liquid becomes entrapped between two solid interfaces. In combination with the presence of tensile residual stress, this favors the occurrence of solidification cracking. c) Two examples of solidification cracks observed during the *operando* experiments (Point A in Fig. 1, and Point C in Fig. S7 in the Supplementary materials).

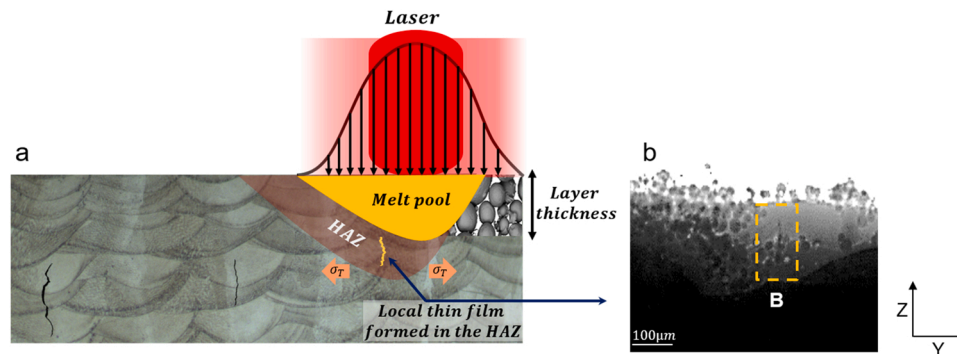


**Fig. 9.** a) Schematic view of liquation cracking in the HAZ of the melt pool, and b) an example of observed liquation crack during the *operando* experiment (Point B in Fig. 4c.).

provides a broad range of information on various critical transient events that are beyond the scope of this paper, e.g. pore formation, melt pool dynamics, or spatter ejection. Hence, this set-up could be used for process optimization of different metals and alloys, validation of thermomechanical simulations and/or microstructure evolution models, and development of new material compositions better designed for L-PBF.

#### CRediT authorship contribution statement

**Eric Boillat:** Visualization, Software, Methodology. **Navid Sohrabi:** Methodology, Investigation, Formal analysis, Data curation. **Federica Marone:** Writing – original draft, Visualization, Software, Resources, Methodology, Investigation. **Daniel Grolimund:** Resources, Formal analysis, Data curation. **Helena Van Swygenhoven:** Writing – review & editing, Supervision, Project administration, Methodology, Funding acquisition, Conceptualization. **Logé Roland E.:** Writing – review & editing, Validation, Supervision, Project administration, Methodology, Funding acquisition, Conceptualization. **Hossein Ghasemi-Tabasi:** Writing – review & editing, Writing – original draft, Visualization, Validation, Software, Resources, Methodology, Investigation, Formal

analysis, Data curation, Conceptualization. **de Formanoir Charlotte:** Writing – review & editing, Writing – original draft, Validation, Investigation, Conceptualization. **Van Petegem Steven:** Writing – original draft, Software, Project administration, Methodology, Formal analysis, Data curation, Conceptualization. **Jamasp Jhabvala:** Writing – review & editing, Validation, Supervision, Methodology, Investigation, Conceptualization. **Samy Hocine:** Writing – original draft, Resources, Investigation, Data curation.

#### Declaration of Competing Interest

The authors declare that they have no known competing financial interests or personal relationships that could have appeared to influence the work reported in this paper.

#### Acknowledgments

This work was supported by (1) the PREcision Additive Manufacturing of Precious metals Alloys (PREAMPA) project, funded by the ETH Board and the Swiss watch and precious metals industry; (2) the Additive Manufacturing and Metallic Microstructures (AM3) project,

funded by the Competence Center for Materials Science and Technology (CCMX) and the Swiss Watch and Precious Metals Industry. We acknowledge the Paul Scherrer Institut, Villigen, Switzerland for the provision of synchrotron radiation beamtime at the TOMCAT and microXAS beamlines of the SLS. The authors kindly thank Dr. Christian Leinenbach and Dr. Seth Griffiths at Swiss Federal Laboratories for Materials Science and Technology (Empa) for providing the CM247LC powder. Special thanks to Dr. Milad Hamidi Nasab at EPFL for helping us in post processing and image analysis of the *operando* experimental data. The generous support of PX Group to the LMTM laboratory is also highly acknowledged.

## Appendix A. Supporting information

Supplementary data associated with this article can be found in the online version at [doi:10.1016/j.addma.2022.102619](https://doi.org/10.1016/j.addma.2022.102619).

## References

- [1] A. Gisario, M. Kazarian, F. Martina, M. Mehrpouya, Metal additive manufacturing in the commercial aviation industry: a review, *J. Manuf. Syst.* 53 (2019) 124–149, <https://doi.org/10.1016/j.jmsys.2019.08.005>.
- [2] T. DebRoy, H.L. Wei, J.S. Zuback, T. Mukherjee, J.W. Elmer, J.O. Milewski, A. M. Beese, A. Wilson-Heid, A. De, W. Zhang, Additive manufacturing of metallic components – process, structure and properties, *Prog. Mater. Sci.* 92 (2018) 112–224, <https://doi.org/10.1016/j.pmatsci.2017.10.001>.
- [3] P.A. Hooper, Melt pool temperature and cooling rates in laser powder bed fusion, *Addit. Manuf.* 22 (2018) 548–559, <https://doi.org/10.1016/j.addma.2018.05.032>.
- [4] V. Thampy, A.Y. Fong, N.P. Calt, J. Wang, A.A. Martin, P.J. Depond, A.M. Kiss, G. Guss, Q. Xing, R.T. Ott, A. van Buuren, M.F. Toney, J.N. Weker, M.J. Kramer, M. J. Matthews, C.J. Tassone, K.H. Stone, Subsurface cooling rates and microstructural response during laser based metal additive manufacturing, *Sci. Rep.* 10 (2020) 1–9, <https://doi.org/10.1038/s41598-020-58598-z>.
- [5] M. Opprecht, J.-P. Garandet, G. Roux, C. Flament, M. Soulier, A solution to the hot cracking problem for aluminium alloys manufactured by laser beam melting, *Acta Mater.* 197 (2020) 40–53, <https://doi.org/10.1016/j.actamat.2020.07.015>.
- [6] N.J. Harrison, I. Todd, K. Mumtaz, Reduction of micro-cracking in nickel superalloys processed by Selective Laser Melting: a fundamental alloy design approach, *Acta Mater.* 94 (2015) 59–68, <https://doi.org/10.1016/j.actamat.2015.04.035>.
- [7] G.S. Reddy, K. Saurabh, D.M. Krishna, Numerical simulation of directionally solidified CM247LC high pressure turbine blade, in: *Materials Today: Proceedings*, Elsevier Ltd, 2017, pp. 7820–7830, <https://doi.org/10.1016/j.matpr.2017.07.117>.
- [8] K. Prasad, R. Sarkar, K. Gopinath, Role of shrinkage pores, carbides on cyclic deformation behaviour of conventionally cast nickel base superalloy CM247LC® at 870°C, *Mater. Sci. Eng. A* 654 (2016) 381–389, <https://doi.org/10.1016/j.msea.2015.12.054>.
- [9] S. Griffiths, H. Ghasemi-Tabasi, A. De Luca, J. Pado, S.S. Joglekar, J. Jhabvala, R. E. Logé, C. Leinenbach, Influence of Hf on the heat treatment response of additively manufactured Ni-base superalloy CM247LC, *Mater. Charact.* 171 (2021), 110815, <https://doi.org/10.1016/j.matchar.2020.110815>.
- [10] Y.T. Tang, C. Panwisawas, J.N. Ghoussoub, Y. Gong, J.W.G. Clark, A.A.N. Németh, D.G. McCartney, R.C. Reed, Alloys-by-design: Application to new superalloys for additive manufacturing, *Acta Mater.* 202 (2021) 417–436, <https://doi.org/10.1016/j.actamat.2020.09.023>.
- [11] J.N.D.J.C. Lippold, S.D. Kiser, *Welding Metallurgy and Weldability of Nickel-base Alloys*, Wiley, 2009.
- [12] J.L. Caron, J.W. Sowards, *Weldability of Nickel-Base Alloys*, Elsevier, 2014, <https://doi.org/10.1016/B978-0-08-096532-1.00615-4>.
- [13] N. Kalentics, R. Sohrabi, H.G. Tabasi, S. Griffiths, J. Jhabvala, C. Leinenbach, A. Burn, R.E. Logé, Healing cracks in selective laser melting by 3D laser shock peening, *Addit. Manuf.* 30 (2019), 100881, <https://doi.org/10.1016/j.addma.2019.100881>.
- [14] S. Griffiths, H. Ghasemi Tabasi, T. Ivas, X. Maeder, A. De Luca, K. Zwiack, R. Wróbel, J. Jhabvala, R.E. Logé, C. Leinenbach, Combining alloy and process modification for micro-crack mitigation in an additively manufactured Ni-base superalloy, *Addit. Manuf.* 36 (2020), 101443, <https://doi.org/10.1016/j.addma.2020.101443>.
- [15] V.D. Divya, R. Muñoz-Moreno, O.M.D.M. Messé, J.S. Barnard, S. Baker, T. Illston, H.J. Stone, Microstructure of selective laser melted CM247LC nickel-based superalloy and its evolution through heat treatment, *Mater. Charact.* 114 (2016) 62–74, <https://doi.org/10.1016/j.matchar.2016.02.004>.
- [16] L.N. Carter, M.M. Attallah, R.C. Reed, Laser powder bed fabrication of nickel-base superalloys: influence of parameters; characterisation, quantification and mitigation of cracking, *Superalloys 2012* (2012) 577–586, <https://doi.org/10.1002/9781118516430.ch64>.
- [17] L.N. Carter, C. Martin, P.J. Withers, M.M. Attallah, The influence of the laser scan strategy on grain structure and cracking behaviour in SLM powder-bed fabricated nickel superalloy, *J. Alloy. Compd.* 615 (2014) 338–347, <https://doi.org/10.1016/j.jallcom.2014.06.172>.
- [18] X. Wang, L.N. Carter, B. Pang, M.M. Attallah, M.H. Loretto, Microstructure and yield strength of SLM-fabricated CM247LC Ni-Superalloy, *Acta Mater.* 128 (2017) 87–95, <https://doi.org/10.1016/j.actamat.2017.02.007>.
- [19] H. Hyer, L. Zhou, A. Mehta, S. Park, T. Huynh, S. Song, Y. Bai, K. Cho, B. McWilliams, Y. Sohn, Composition-dependent solidification cracking of aluminum-silicon alloys during laser powder bed fusion, *Acta Mater.* 208 (2021), 116698, <https://doi.org/10.1016/j.actamat.2021.116698>.
- [20] T. Soysal, S. Kou, A simple test for assessing solidification cracking susceptibility and checking validity of susceptibility prediction, *Acta Mater.* 143 (2018) 181–197, <https://doi.org/10.1016/j.actamat.2017.09.065>.
- [21] M. Qian, J.C. Lippold, The effect of annealing twin-generated special grain boundaries on HAZ liquation cracking of nickel-base superalloys, *Acta Mater.* 51 (2003) 3351–3361, [https://doi.org/10.1016/S1359-6454\(03\)00090-9](https://doi.org/10.1016/S1359-6454(03)00090-9).
- [22] A.A.N. Németh, D.J. Crudden, D.E.J. Armstrong, D.M. Collins, K. Li, A. J. Wilkinson, C.R.M. Grover, R.C. Reed, Environmentally-assisted grain boundary attack as a mechanism of embrittlement in a nickel-based superalloy, *Acta Mater.* 126 (2017) 361–371, <https://doi.org/10.1016/j.actamat.2016.12.039>.
- [23] M. Cloots, P.J. Uggowitzer, K. Wegener, Investigations on the microstructure and crack formation of IN738LC samples processed by selective laser melting using Gaussian and doughnut profiles, *Mater. Des.* 89 (2016) 770–784, <https://doi.org/10.1016/j.matdes.2015.10.027>.
- [24] B. Vrancken, R.K. Ganeriwala, M.J. Matthews, Analysis of laser-induced microcracking in tungsten under additive manufacturing conditions: Experiment and simulation, *Acta Mater.* 194 (2020) 464–472, <https://doi.org/10.1016/j.actamat.2020.04.060>.
- [25] Z. Jia, P. Zhang, Z. Yu, D. Wu, Y. Tian, H. Yan, Evidence of solidification crack propagation in pulsed laser welding of aluminum alloy, *Opt. Express* 29 (2021) 18495–18501, <https://doi.org/10.1364/OE.422369>.
- [26] Q. Guo, C. Zhao, M. Qu, L. Xiong, L.I. Escano, S.M.H. Hojjatzadeh, N.D. Parab, K. Fezzaa, W. Everhart, T. Sun, L. Chen, In-situ characterization and quantification of melt pool variation under constant input energy density in laser powder bed fusion additive manufacturing process, *Addit. Manuf.* 28 (2019) 600–609, <https://doi.org/10.1016/j.addma.2019.04.021>.
- [27] C. Zhao, K. Fezzaa, R.W. Cunningham, H. Wen, F. De Carlo, L. Chen, A.D. Rollett, T. Sun, Real-time monitoring of laser powder bed fusion process using high-speed X-ray imaging and diffraction, *Sci. Rep.* 7 (2017) 3602, <https://doi.org/10.1038/s41598-017-03761-2>.
- [28] N.P. Calt, A.A. Martin, J.A. Hammons, M.H. Nielsen, T.T. Roehling, K. Fezzaa, M. J. Matthews, J.R. Jeffries, T.M. Willey, J.R.I. Lee, Pressure dependence of the laser-metal interaction under laser powder bed fusion conditions probed by in situ X-ray imaging, *Addit. Manuf.* 32 (2020), 101084, <https://doi.org/10.1016/j.addma.2020.101084>.
- [29] A.A. Martin, N.P. Calt, J.A. Hammons, S.A. Khairallah, M.H. Nielsen, R. M. Shuttlesworth, N. Sinclair, M.J. Matthews, J.R. Jeffries, T.M. Willey, J.R.I. Lee, Ultrafast dynamics of laser-metal interactions in additive manufacturing alloys captured by in situ X-ray imaging, *Mater. Today Adv.* 1 (2019), 100002, <https://doi.org/10.1016/j.mtadv.2019.01.001>.
- [30] R. Cunningham, C. Zhao, N. Parab, C. Kantzos, J. Pauza, K. Fezzaa, T. Sun, A. D. Rollett, Keyhole threshold and morphology in laser melting revealed by ultrahigh-speed x-ray imaging, *Science* 363 (2019) 849–852, <https://doi.org/10.1126/science.aav4687>.
- [31] C.L.A. Leung, S. Marussi, R.C. Atwood, M. Towrie, P.J. Withers, P.D. Lee, In situ X-ray imaging of defect and molten pool dynamics in laser additive manufacturing, *Nat. Commun.* 9 (2018) 1355, <https://doi.org/10.1038/s41467-018-03734-7>.
- [32] N.D. Parab, C. Zhao, R. Cunningham, L.I. Escano, K. Fezzaa, W. Everhart, A. D. Rollett, L. Chen, T. Sun, Ultrafast X-ray imaging of laser-metal additive manufacturing processes, *J. Synchrotron Radiat.* 25 (2018) 1467–1477, <https://doi.org/10.1107/S1600577518009554>.
- [33] T. Sun, Probing ultrafast dynamics in laser powder bed fusion using high-speed X-ray imaging: a review of research at the advanced photon source, *Jom* 72 (2020) 999–1008, <https://doi.org/10.1007/s11837-020-04015-9>.
- [34] C. Zhao, N.D. Parab, X. Li, K. Fezzaa, W. Tan, A.D. Rollett, T. Sun, Critical instability at moving keyhole tip generates porosity in laser melting, *Science* 1086 (2020) 1080–1086.
- [35] S.J. Wolff, S. Webster, N.D. Parab, B. Aronson, B. Gould, A. Greco, T. Sun, In-situ observations of directed energy deposition additive manufacturing using high-speed X-ray imaging, *Jom* 73 (2021) 189–200, <https://doi.org/10.1007/s11837-020-04469-x>.
- [36] B.J. Simonds, J. Tanner, A. Artusio-Glimpse, P.A. Williams, N. Parab, C. Zhao, T. Sun, Simultaneous high-speed x-ray transmission imaging and absolute dynamic absorbance measurements during high-power laser-metal processing, *Procedia CIRP* 94 (2020) 775–779, <https://doi.org/10.1016/j.procir.2020.09.135>.
- [37] S.M.H. Hojjatzadeh, N.D. Parab, Q. Guo, M. Qu, L. Xiong, C. Zhao, L.I. Escano, K. Fezzaa, W. Everhart, T. Sun, L. Chen, Direct observation of pore formation mechanisms during LPBF additive manufacturing process and high energy density laser welding, *Int. J. Mach. Tools Manuf.* 153 (2020), 103555, <https://doi.org/10.1016/j.ijmachtools.2020.103555>.
- [38] Q. Guo, C. Zhao, M. Qu, L. Xiong, S.M.H. Hojjatzadeh, L.I. Escano, N.D. Parab, K. Fezzaa, T. Sun, L. Chen, In-situ full-field mapping of melt flow dynamics in laser metal additive manufacturing, *Addit. Manuf.* 31 (2020), 100939, <https://doi.org/10.1016/j.addma.2019.100939>.
- [39] Y. Chen, S.J. Clark, C.L.A. Leung, L. Sinclair, S. Marussi, M.P. Olbinado, E. Boller, A. Rack, I. Todd, P.D. Lee, In-situ Synchrotron imaging of keyhole mode multi-layer laser powder bed fusion additive manufacturing, *Appl. Mater. Today* 20 (2020), 100650, <https://doi.org/10.1016/j.apmt.2020.100650>.

- [40] Y. Chen, S.J. Clark, L. Sinclair, C.L.A. Leung, S. Marussi, T. Connolly, R. C. Atwood, G.J. Baxter, M.A. Jones, I. Todd, P.D. Lee, Synchrotron X-ray imaging of directed energy deposition additive manufacturing of titanium alloy Ti-6242, *Addit. Manuf.* 41 (2021), 101969, <https://doi.org/10.1016/j.addma.2021.101969>.
- [41] Z. Gan, O.L. Kafka, N. Parab, C. Zhao, L. Fang, O. Heinonen, T. Sun, W.K. Liu, Universal scaling laws of keyhole stability and porosity in 3D printing of metals, *Nat. Commun.* 12 (2021) 2379, <https://doi.org/10.1038/s41467-021-22704-0>.
- [42] A.A. Martin, N.P. Calt, S.A. Khairallah, J. Wang, P.J. Depond, A.Y. Fong, V. Thampy, G.M. Guss, A.M. Kiss, K.H. Stone, C.J. Tassone, J. Nelson Weker, M. F. Toney, T. van Buuren, M.J. Matthews, Dynamics of pore formation during laser powder bed fusion additive manufacturing, *Nat. Commun.* 10 (2019) 1–10, <https://doi.org/10.1038/s41467-019-10009-2>.
- [43] S.M.H. Hojjatzadeh, N.D. Parab, W. Yan, Q. Guo, L. Xiong, C. Zhao, M. Qu, L. I. Escano, X. Xiao, K. Fezzaa, W. Everhart, T. Sun, L. Chen, Pore elimination mechanisms during 3D printing of metals, *Nat. Commun.* 10 (2019) 1–8, <https://doi.org/10.1038/s41467-019-10973-9>.
- [44] S. Shevchik, T. Le-Quang, B. Meylan, F.V. Farahani, M.P. Olbinado, A. Rack, G. Masinelli, C. Leinenbach, K. Wasmer, Supervised deep learning for real-time quality monitoring of laser welding with X-ray radiographic guidance, *Sci. Rep.* 10 (2020) 1–12, <https://doi.org/10.1038/s41598-020-60294-x>.
- [45] L. Sinclair, C.L.A. Leung, S. Marussi, S.J. Clark, Y. Chen, M.P. Olbinado, A. Rack, J. Gardy, G.J. Baxter, P.D. Lee, In situ radiographic and ex situ tomographic analysis of pore interactions during multilayer builds in laser powder bed fusion, *Addit. Manuf.* 36 (2020), 101512, <https://doi.org/10.1016/j.addma.2020.101512>.
- [46] Z.A. Young, Q. Guo, N.D. Parab, C. Zhao, M. Qu, L.I. Escano, K. Fezzaa, W. Everhart, T. Sun, L. Chen, Types of spatter and their features and formation mechanisms in laser powder bed fusion additive manufacturing process, *Addit. Manuf.* 36 (2020), 101438, <https://doi.org/10.1016/j.addma.2020.101438>.
- [47] Q. Guo, C. Zhao, L.I. Escano, Z. Young, L. Xiong, K. Fezzaa, W. Everhart, B. Brown, T. Sun, L. Chen, Transient dynamics of powder spattering in laser powder bed fusion additive manufacturing process revealed by in-situ high-speed high-energy x-ray imaging, *Acta Mater.* 151 (2018) 169–180, <https://doi.org/10.1016/j.actamat.2018.03.036>.
- [48] L.I. Escano, N.D. Parab, L. Xiong, Q. Guo, C. Zhao, T. Sun, L. Chen, Investigating powder spreading dynamics in additive manufacturing processes by in-situ high-speed X-ray imaging, *Synchrotron Radiat. N.* 32 (2019) 9–13, <https://doi.org/10.1080/08940886.2019.1582281>.
- [49] J. Yin, D. Wang, L. Yang, H. Wei, P. Dong, L. Ke, G. Wang, H. Zhu, X. Zeng, Correlation between forming quality and spatter dynamics in laser powder bed fusion, *Addit. Manuf.* 31 (2020), 100958, <https://doi.org/10.1016/j.addma.2019.100958>.
- [50] S.J. Wolff, H. Wu, N. Parab, C. Zhao, K.F. Ehmann, T. Sun, J. Cao, In-situ high-speed X-ray imaging of piezo-driven directed energy deposition additive manufacturing, *Sci. Rep.* 9 (2019) 1–14, <https://doi.org/10.1038/s41598-018-36678-5>.
- [51] M. Yakout, I. Phillips, M.A. Elbestawi, Q. Fang, In-situ monitoring and detection of spatter agglomeration and delamination during laser-based powder bed fusion of Invar 36, *Opt. Laser Technol.* 136 (2021), 106741, <https://doi.org/10.1016/j.optlastec.2020.106741>.
- [52] P.-J. Chiang, R. Jiang, R. Cunningham, N. Parab, C. Zhao, K. Fezzaa, T. Sun, A. D. Rollett, in: J. Nakano, P.C. Pistorius, C. Tamerler, H. Yasuda, Z. Zhang, N. Dogan, W. Wang, N. Saito, B. Webler (Eds.), *In Situ Characterization of Hot Cracking Using Dynamic X-Ray Radiography BT - Advanced Real Time Imaging II*, Springer International Publishing, Cham, 2019, pp. 77–85.
- [53] N. Kouraytem, P.-J. Chiang, R. Jiang, C. Kantzos, J. Pauza, R. Cunningham, Z. Wu, G. Tang, N. Parab, C. Zhao, K. Fezzaa, T. Sun, A.D. Rollett, Solidification crack propagation and morphology dependence on processing parameters in AA6061 from ultra-high-speed x-ray visualization, *Additive Manufacturing*, 2021, <https://doi.org/10.1016/j.addma.2021.101959>.
- [54] S. Hocine, H. Van Swygenhoven, S. Van Petegem, C.S.T. Chang, T. Maimaitiyili, G. Tinti, D. Ferreira Sanchez, D. Grolimund, N. Casati, Operando X-ray diffraction during laser 3D printing, *Mater. Today* 34 (2020) 30–40, <https://doi.org/10.1016/j.mattod.2019.10.001>.
- [55] S. Hocine, S. Van Petegem, U. Frommherz, G. Tinti, N. Casati, D. Grolimund, H. Van Swygenhoven, A miniaturized selective laser melting device for operando X-ray diffraction studies, *Addit. Manuf.* 34 (2020), 101194, <https://doi.org/10.1016/j.addma.2020.101194>.
- [56] M. Bührer, M. Stampanoni, X. Rochet, F. Buchi, J. Eller, F. Marone, High-numerical-aperture microscope optics for time-resolved experiments, *J. Synchrotron Radiat.* 26 (2019) 1161–1172.
- [57] R. Mokso, C.M. Schlepütz, G. Theidel, H. Billich, E. Schmid, T. Celcer, G. Mikuljan, L. Sala, F. Marone, N. Schlumpf, M. Stampanoni, GigaFroST: the gigabit fast readout system for tomography, *J. Synchrotron Radiat.* 24 (2017) 1250–1259.
- [58] S. Ly, A.M. Rubenchik, S.A. Khairallah, G. Guss, M.J. Matthews, Metal vapor micro-jet controls material redistribution in laser powder bed fusion additive manufacturing, *Sci. Rep.* 7 (2017) 1–12, <https://doi.org/10.1038/s41598-017-04237-z>.
- [59] R. Rajendran, V. Petley, B. Rehmer, Dynamic elastic properties of aero-engine metallic isotropic materials, *Proceedings of the Institution of Mechanical Engineers, Part L: J. Mater.: Des. Appl.* 227 (2013) 243–249, <https://doi.org/10.1177/1464420712454071>.
- [60] S.A. Oh, R.E. Lim, J.W. Aroh, A.C. Chuang, B.J. Gould, B. Amin-Ahmadi, J. V. Bernier, T. Sun, P.C. Pistorius, R.M. Suter, A.D. Rollett, High speed synchrotron X-ray diffraction experiments resolve microstructure and phase transformation in laser processed Ti-6Al-4V, *Mater. Res. Lett.* 9 (2021) 429–436, <https://doi.org/10.1080/21663831.2021.1966537>.
- [61] H. Ghasemi-Tabasi, J. Jhabvala, E. Boillat, T. Ivas, R. Drissi-Daoudi, R.E. Logé, An effective rule for translating optimal selective laser melting processing parameters from one material to another, *Addit. Manuf.* 36 (2020), 101496, <https://doi.org/10.1016/j.addma.2020.101496>.
- [62] H. Ghasemi Tabasi, Understanding Thermomechanical Treatments Induced by Laser Powder Bed Fusion Process, EPFL PP - Lausanne, n.d. <https://doi.org/10.5075/epfl-thesis-8958>.
- [63] R.E. Aune, L. Battezzati, R. Brooks, I. Egry, H.J. Fecht, J.P. Garandet, M. Hayashi, K.C. Mills, A. Passerone, P.N. Quedest, E. Ricci, F. Schmidt-Hohagen, S. Seetharaman, B. Vinet, R.K. Wunderlich, Thermophysical properties of IN738LC, MM247LC and CMSX-4 in the liquid and high temperature solid phase, in: *Proceedings of the International Symposium on Superalloys and Various Derivatives*, 2005: pp. 467–476. <https://doi.org/10.7449/2005/superalloys.2005.467.476>.
- [64] R. Przeliorz, M. Góral, Heat resistance and heat capacity of the selected nickel superalloys, *Solid State Phenom.* 227 (2015) 329–332, <https://doi.org/10.4028/www.scientific.net/SSP.227.329>.
- [65] E.B. Curry, S. Sahoo, C. Herrera, I. Sochnikov, S. Pamir Alpaly, R.J. Hebert, B. G. Willis, J. Qi, J.N. Hancock, Optical response of nickel-based superalloy Inconel-718 for applications in additive manufacturing, *J. Appl. Phys.* 127 (2020), 245111, <https://doi.org/10.1063/5.0006006>.
- [66] L. Cao, X. Yuan, Study on the numerical simulation of the SLM molten pool dynamic behavior of a nickel-based superalloy on the workpiece scale, *Materials* 12 (2019) 2272, <https://doi.org/10.3390/ma12142272>.
- [67] E. Chauvet, P. Kontis, E.A. Jägle, B. Gault, D. Raabe, C. Tassin, J.J. Blandin, R. Dendievel, B. Vayre, S. Abed, G. Martin, Hot cracking mechanism affecting a non-weldable Ni-based superalloy produced by selective electron Beam Melting, *Acta Mater.* 142 (2018) 82–94, <https://doi.org/10.1016/j.actamat.2017.09.047>.
- [68] A. Sonawane, G. Roux, J.J. Blandin, A. Despres, G. Martin, Cracking mechanism and its sensitivity to processing conditions during laser powder bed fusion of a structural aluminum alloy, *Materialia* 15 (2021), 100976, <https://doi.org/10.1016/j.mtl.2020.100976>.
- [69] N. Wang, S. Mokadem, M. Rappaz, W. Kurz, Solidification cracking of superalloy single- and bi-crystals, *Acta Mater.* 52 (2004) 3173–3182, <https://doi.org/10.1016/j.actamat.2004.03.047>.
- [70] T. Polivnikova, Study and modelling of the melt pool dynamics during Selective Laser Sintering and Melting, EPFL, 2015.
- [71] I. Serrano-Munoz, T. Mishurova, T. Thiede, M. Sprengel, A. Kromm, N. Nadammal, G. Nolze, R. Saliwan-Neumann, A. Evans, G. Bruno, The residual stress in as-built Laser Powder Bed Fusion IN718 alloy as a consequence of the scanning strategy induced microstructure, *Sci. Rep.* 10 (2020) 14645, <https://doi.org/10.1038/s41598-020-71112-9>.
- [72] A.V. Gusarov, M. Pavlov, I. Smurov, Residual stresses at laser surface remelting and additive manufacturing, *Phys. Procedia* 12 (2011) 248–254, <https://doi.org/10.1016/j.phpro.2011.03.032>.
- [73] J. Ding, P. Colegrove, J. Mehnert, S. Ganguly, P.M.S. Almeida, F. Wang, S. Williams, Thermo-mechanical analysis of Wire and Arc Additive Layer Manufacturing process on large multi-layer parts, *Comput. Mater. Sci.* 50 (2011) 3315–3322, <https://doi.org/10.1016/j.commatsci.2011.06.023>.
- [74] F. Brückner, D. Lepski, E. Beyer, Modeling the influence of process parameters and additional heat sources on residual stresses in laser cladding, *J. Therm. Spray. Technol.* 16 (2007) 355–373, <https://doi.org/10.1007/s11666-007-9026-7>.
- [75] S. Zou, H. Xiao, F. Ye, Z. Li, W. Tang, F. Zhu, C. Chen, C. Zhu, Numerical analysis of the effect of the scan strategy on the residual stress in the multi-laser selective laser melting, *Results Phys.* 16 (2020), 103005, <https://doi.org/10.1016/j.rinp.2020.103005>.
- [76] J. Song, W. Wu, L. Zhang, B. He, L. Lu, X. Ni, Q. Long, G. Zhu, Role of scanning strategy on residual stress distribution in Ti-6Al-4V alloy prepared by selective laser melting, *Optik* 170 (2018) 342–352, <https://doi.org/10.1016/j.jlejo.2018.05.128>.
- [77] J. Jhabvala, E. Boillat, T. Antignac, R. Glardon, On the effect of scanning strategies in the selective laser melting process, *Virtual Phys. Prototyp.* 5 (2010) 99–109, <https://doi.org/10.1080/17452751003688368>.
- [78] W. Zhang, M. Tong, N.M. Harrison, Scanning strategies effect on temperature, residual stress and deformation by multi-laser beam powder bed fusion manufacturing, *Addit. Manuf.* 36 (2020), 101507, <https://doi.org/10.1016/j.addma.2020.101507>.
- [79] J. Draxler, J. Edborg, J. Andersson, L.-E. Lindgren, Modeling and simulation of weld solidification cracking part II, *Weld. World* 63 (2019) 1503–1519, <https://doi.org/10.1007/s40194-019-00761-w>.
- [80] M. Rappaz, J.-M. Drezet, M. Gremaud, A new hot-tearing criterion, *Metall. Mater. Trans. A* 30 (1999) 449–455, <https://doi.org/10.1007/s11661-999-0334-z>.
- [81] A. Sonawane, G. Roux, J.J. Blandin, A. Despres, G. Martin, Cracking mechanism and its sensitivity to processing conditions during laser powder bed fusion of a structural aluminum alloy, *Materialia* 15 (2021), 100976, <https://doi.org/10.1016/j.mtl.2020.100976>.
- [82] M. Ramsperger, R.F. Singer, C. Körner, Microstructure of the nickel-base superalloy CMSX-4 fabricated by selective electron beam melting, *Metall. Mater. Trans. A* 47 (2016) 1469–1480, <https://doi.org/10.1007/s11661-015-3300-y>.
- [83] Y.-C. Hagedorn, J. Risse, W. Meiners, N. Pirch, K. Wissenbach, R. Poprawe, Processing of nickel based superalloy MAR M-247 by means of High Temperature - Selective Laser Melting (HT - SLM), in: *High Value Manufacturing: Advanced Research in Virtual and Rapid Prototyping - Proceedings of the 6th International Conference on Advanced Research and Rapid Prototyping, VR@P 2013*, 2014: pp. 291–295.